Fourier transform distribution function of relaxation times; application and limitations

Bernard A. Boukamp

University of Twente, Faculty of Science and Technology & MESA+ Institute for Nanotechnology, P.O.Box 217, 7500AE Enschede, The Netherlands

ABSTRACT

A simple Fourier transform (FT) method is presented for obtaining a Distribution Function of Relaxation Times (DFRT) for electrochemical impedance spectroscopy (EIS) data. By using a special data extension procedure the FT is performed over the range from $-\infty \leq \ln\omega \leq +\infty$. The integration procedure is analytic in the end regions, otherwise a quadratic interpolation is used. For the necessary windowing of the first FT result, a special Tanh window function is used, which shows better results than the well-known Hann window function. An alternative approach, based on a complex nonlinear least squares (CNLS) fit of a linear sequence of (RQ)'s, provides the DFRT directly, but often significantly deviating from the FT-DFRT. With several examples the usefulness of a DFRT in impedance analysis is tested. The main conclusion is that the visibility in the DFRT of separate dispersive contributions strongly depends on the associated resistance and the width of the distribution. 'Near equal strength' dispersive contributions show up in the DFRT, where the area under the DFRT-peak represents the 'strength' or resistance. But small peaks with a large FWHM are lost, although these can easily be identified in a CNLS-fit.

A comparison between the finite length Warburg (FLW) and the almost identical Gerischer impedance shows a clear difference in the DFRT. Indications are found that the characteristic Gerischer DFRT might be distinguishable in real measurement DFRT's.

In cooperation with an external group a brief test with an adaptive genetic evolution method showed promising results for a direct definition of a DFRT. In this process the reconstructed impedance is matched to the actual measurement.

© 2014 Elsevier Ltd. All rights reserved.

1. Introduction

Electrochemical Impedance Spectroscopy (EIS) has come a long way since its introduction in wet-electrochemical research by Sluyters and Sluyters-Rehbach in the sixties of the last century [1,2]. In the seventies it was recognized by the solid state research community as an important tool for studying ionic conductivity and electrode effects. It proved to be far superior to the, then standard, practice of single frequency measurements. In that time it moved from manual graphical analysis of simple systems to computer aided analysis for progressively more complex systems. Notably Macdonald [3,4], Boukamp [5,6] and others [7,8] have contributed to this rapid expansion with the development of complex nonlinear least squares (CNLS) analysis programs.

A recent overview of the status of impedance data analysis, based on the concept of 'Equivalent Circuits' (abbreviated 'EqC'), has been presented in ref. [9]. New directions that did not involve electrical analogs were also receiving some attention [10], but most publications relied on an equivalent circuit interpretation which was based on a limited set of direct electrical relations (R, C, L) and more complex transfer functions derived from the Laplace transform of (bounded) diffusion equations (Warburg types [11–13] and Gerischer [14,15] or chemical impedance [16]) as well as empirical relations, e.g. the constant phase element, or CPE [17], and the Havriliak-Negami response function [18]. Since then several books on impedance spectroscopy have become available, notably by Barsoukov and Macdonald [19], Orazem and Tribollet [20] and Lvovich [21]. The most recent book by Lasia [22] presents an excellent introduction into EIS, its mathematics and data analysis.

In solid oxide fuel cell (SOFC) research EIS has played an important role in characterizing ionic transport processes in separate anode, cathode or electrolyte studies. Its application to complete cells, however, has created significant challenges as it becomes difficult to breakdown the frequency dispersion of the impedance in the separate anode and cathode processes. This is caused by closely spaced time constants for the various electrochemical processes in both electrodes.

In this area of research the definition of a distribution function of relaxation times (DFRT) has been found to be useful for analyzing the measured impedance response. This DFRT, i.e. $R_p \cdot G$ (τ), is found from the inversion of the following well-known equation:

$$Z(\omega_i) = R_\infty + R_{pol} \int_0^\infty \frac{\gamma(\tau)}{1 + j\omega_i \tau} \mathrm{d}\tau$$
$$= R_\infty + R_{pol} \int_{-\infty}^\infty \frac{G(\tau)}{1 + j\omega_i \tau} \mathrm{dln}\tau \qquad (1)$$

with: $G(\tau) = \tau \cdot \gamma(\tau)$ and: $\int_{-\infty}^\infty G(\tau)\mathrm{dln}\tau = 1$. R_∞ is the high frequency cut-off resistance and R_{pol} is the polarization resistance, $R_{pol} = R_{dc} - R_\infty$, with R_{dc} the impedance value for $\omega \to 0$. Solving Eq. (1) for $G(\tau)$ is known as an ill-posed inverse problem. Various methods have been devised to obtain a useful representation of G (τ). In a recent publication [23] the research group of Prof. Ivers-Tiffée presented a Fourier transform method which derived the G (τ)-DFRT from the imaginary part of the impedance. This method has been taken as the basis for this study.

Hörlin has proposed and demonstrated the usefulness of the maximum entropy method [24,25] for solving Eq. (1). Apparently this method has received very little attention in the solid state community. Another mathematical procedure is known as the 'Tikhonov regularization' [26]. Both methods require adjustment of the procedure with a 'smoothing parameter'. Too little smoothing yields unrealistic oscillations and superfluous small peaks, too much results in a rather smooth curve, suppressing the essential details. Saccoccio et al. [27] have recently presented an automated optimization method for the Tikhonov regularization.

But the Fourier de-convolution method also needs a separate, adjustable windowing function, as will be demonstrated below. Despite these complications, it seems that transforming impedance measurements to DFRT's is becoming a new trend in EIS-analysis. In this publication we will take a closer look at the possibilities and limitations of DFRT analysis. This will be based on four simple questions, each illustrated with a specific impedance problem:

1. How accurately or uniquely does a DFRT describe the impedance measurement?

2. Can a DFRT indicate the presence of special transfer functions, e.g. the finite length Warburg (FLW, [11]) or the Gerischer [14].

3. Can it accurately predict the number of circuit parameters, based on observed time constants?

4. Can it be a substitute analysis method for EIS-data for which no simple EqC exists?

The first question will be illustrated with the simulated data presented by Schichlein et al. [23]. This will allow for a validation of our Fourier de-convolution method, which is based on the principles described in that publication. The difference in appearance of DFRT's for comparable FLW and Gerischer functions will be used for inspection of the second question.

An already published complex EIS analysis on $PbZr_{0.53}Ti_{0.47}O_3$ (PZT, a mixed conducting piezoelectric Perovskite [28,29]) is used to investigate the third question. Temperature and pO_2 dependent measurements could be resolved with one equivalent circuit with up to 12 independent parameters. But arriving at this EqC was not a trivial task, as detailed in ref. [29].

The final question is tested with the impedance of a $La_{0.6}Sr_{0.4}Co_{0.2}Fe_{0.8}O_{3-\delta}$ cathode (LSCF). It was observed that the sintering temperature of the screen-printed cathode had a strong effect on the area specific resistance (ASR) [30]. A sintering temperature of $1200\,^\circ C$ resulted in an optimal ASR, while after sintering at $1300\,^\circ C$, a significantly larger ASR was obtained. The electrode microstructure showed a large number of closed pores with a distribution in pore size. These electrode impedances could not be resolved with a simple EqC; hence the question 'what can

we learn from the DFRT'? In this case the analysis was also carried out by an adaptive genetic evolution algorithm method developed by the group of Tsur [31,32].

Actually measured EIS data have been validated with a Kramers-Kronig test [33]. The results are presented in a so-called residuals graph, a plot of relative differences between the real values and the imaginary values of the data and KK-transform versus log(f), with $\omega = 2\pi f$:

$$\Delta_{re}(\omega_i) = \frac{Z_{dat,re}(\omega_i) - Z_{KK,re}(\omega_i)}{|Z_{dat}(\omega_i)|}, \Delta_{im}(\omega_i)$$
$$= \frac{Z_{dat,im}(\omega_i) - Z_{KK,im}(\omega_i)}{|Z_{dat}(\omega_i)|} \qquad (2)$$

An important check of the validity of a DFRT is its conversion to the impedance representation and comparing it with the measured or originally simulated data in such a residuals graph. Another quality check for fitted data is the *pseudo* χ^2-value (*pseudo*, as χ^2 has not been normalized for the parent distribution of variances). For a CNLS-fit this has been defined as [5]:

$$\chi^2_{CNLS} = \frac{1}{N - M - 1}$$
$$\times \sum_N \frac{(Z_{dat,re}(\omega_i) - Z_{mod,re}(\omega_i))^2 + (Z_{dat,im}(\omega_i) - Z_{mod,im}(\omega_i))^2}{|Z_{mod}(\omega_i)|^2} \qquad (3)$$

Where N is the number of data sets and M the number of adjustable parameters. $Z_{mod}(\omega)$ represents the model function derived from the EqC. For the Kramers-Kronig test a similar pseudo χ^2 has been defined [33]:

$$\chi^2_{KK} = \frac{1}{N} \sum_N \frac{(Z_{dat,re}(\omega_i) - Z_{KK,re}(\omega_i))^2 + (Z_{dat,im}(\omega_i) - Z_{KK,im}(\omega_i))^2}{|Z_{dat}(\omega_i)|^2} \qquad (4)$$

An optimal CNLS-fit has been obtained when the χ^2_{CNLS} -value is close to χ^2_{KK}, i.e. the residuals graph shows mostly the statistical noise. A low value of $\sim 10^{-6}$ generally indicates a very good fit, although for some data sets χ^2-values down to 10^{-8} have been observed. For the comparison of the impedance reconstructed from the DFRT with the original data a χ^2_{diff} is defined. Its definition is analogue to Eq. (4), with $Z_{KK}(\omega)$ replaced by the reconstructed impedance data.

Although the main aim of this contribution is to investigate the possibilities and limits of the Fourier transform DFRT, an alternative method based on a CNLS-fit with a linear series of (RQ) circuits will be used for comparison. Q represents the constant phase element (or CPE) with $Z_Q(\omega) = Y_Q(\omega)^{-1} = [Y_0(j\omega)^n]^{-1}$. Here the circuit description code, as developed by the author, is used [5,9]. The impedance is then fitted to an optimum number of (RQ)'s and (RC)'s so that the residuals graph shows more or less the noise in the data set. Each (RQ) circuit can be directly transformed to a DFRT according to [34,35]:

$$R \cdot G(\tau)_{(RQ)} = \frac{R}{2\pi} \cdot \frac{\sin((1 - n)\pi)}{\cosh(n\ln(\tau/\tau_0)) - \cos((1 - n)\pi)} \qquad (5)$$

with: $\tau_0 = \omega_0^{-1} = \sqrt[n]{RY_0}$. In the case of a pure capacitance, i.e. $n = 1$ for a (RC)-circuit, Eq. (5) transforms into a δ-function. It will be shown, however, that this δ-function can be approximated by a narrow Gaussian distribution:

$$R \cdot G(\tau)_{Gauss} = \frac{R}{W\sqrt{\pi}} e^{-\left(\frac{\ln(\tau/\tau_0)}{W}\right)^2} \qquad (6)$$

where W determines the width of the Gauss function (FWHM = $1.67xW$ on the $\ln\tau$ scale). The introduced error is small when W is kept small (e.g. ~0.15). It allows a visual presentation of the 'strength' (surface area under the curve which is equal to R) of the δ-function. The DFRT is then the sum of all separate contributions:

$$R_p \cdot G(\tau) = \sum_i R_i \cdot G_i(\tau), R_p = \sum_i R_i \tag{7}$$

2. Mathematical procedure

2.1. General approach

The overall procedure follows the outline of Schichlein et al. [23]. Through a change of variables in Eq. (1) a Fredholm integral of the first kind is obtained:

$$Z_{im}(\omega) = -\frac{R_{pol}}{2}\int_{-\infty}^{\infty} G(y-x) \cdot \mathrm{sech}(y)\mathrm{d}y = -\frac{R_{pol}}{2}G(x) * \mathrm{sech}(x) \tag{8}$$

with: $x = \ln(\omega/\omega_0)$ and $y = \ln(\omega\tau)$. ω_0 is the center frequency of the data set, with $\omega_0 = \sqrt{(\omega_{min} \cdot \omega_{max})}$. With a Fourier transform the right-hand side convolution of Eq. (8) is separated into:

$$\overline{G(s)} = -\frac{2}{R_{pol}}\frac{\overline{Z_{im}(s)}}{\overline{\mathrm{sech}(s)}} \tag{9}$$

The right hand side of Eq. (9) represents the first Fourier transform and will be denoted by 'Fourier-1'. A subsequent inverse Fourier transform will then yield the sought DFRT. It is, however, essential to apply a window function to $\overline{G(s)}$ in order to remove the strong oscillations in the end regions of the right hand side of Eq. (9). The width of the window has a significant effect on the form of the DFRT, as will be shown below.

The approach presented in this contribution is based on an approximation of the true Fourier integral of $Z_{im}(\omega)$. This requires an extension of the impedance from $\omega = 0$ to $\omega = \infty$. A simple assumption is that an end-region of the actual measurement is mostly due to a single time constant process. Hence an extrapolation with a R(RQ) circuit for the low and for the high end region is a viable method. This scheme has been used previously in a simple Kramers-Kronig transform test, see ref. [36]. By fitting the R(RQ) extension circuits to a limited data set, e.g. 5–10 data points, a smooth transition to the extension is obtained. A further advantage is that at sufficiently low (or high) frequency this dispersion relation can be simplified to an expression that can be analytically Fourier transformed.

2.2. Analytic low and high frequency Fourier terms

The low frequency extension is given by:

$$Z_{im,low} = -R\frac{R \cdot Y_0\omega^n\sin\frac{n\pi}{2}}{1 + 2R \cdot Y_0\cos\frac{n\pi}{2} + (R \cdot Y_0\omega^n)^2}$$
$$\approx -R^2Y_0\omega^n\sin\frac{n\pi}{2}\Big|_{\omega\to 0} \tag{10}$$

with $Y_Q = Y_0(j\omega)^n$ and R is the resistance in parallel. For low enough frequencies this extension can be approximated by the right most part of Eq. (10) which is used in an analytic Fourier transform between $-\infty$ and x_{ll} (= $\ln\omega_{ll}$). By setting a tolerance, Δ_{low}, for the misfit between left and right part of Eq. (10) the changeover frequency can be established. With:

$$\Delta_{low} = 1 - \frac{1}{1 + 2R \cdot Y_0\cos\frac{n\pi}{2} + (R \cdot Y_0\omega^n)^2} \tag{11}$$

the changeover frequency, ω_{ll}, is obtained:

$$\omega_{ll}^n = \frac{-\cos\frac{n\pi}{2} + \sqrt{\cos^2\frac{n\pi}{2} + \frac{\Delta_{low}}{1-\Delta_{low}}}}{R \cdot Y_0} \approx \frac{\Delta_{low}}{2R \cdot Y_0\cos\frac{n\pi}{2}}\Big|_{\Delta\to 0} \tag{12}$$

Similarly the upper limit frequency, ω_{ul}, can be found for the high frequency extension:

$$Z_{im,high} = -R\frac{R \cdot Y_0\omega^n\sin\frac{n\pi}{2}}{1 + 2R \cdot Y_0\omega^n\cos\frac{n\pi}{2} + (R \cdot Y_0\omega^n)^2}$$
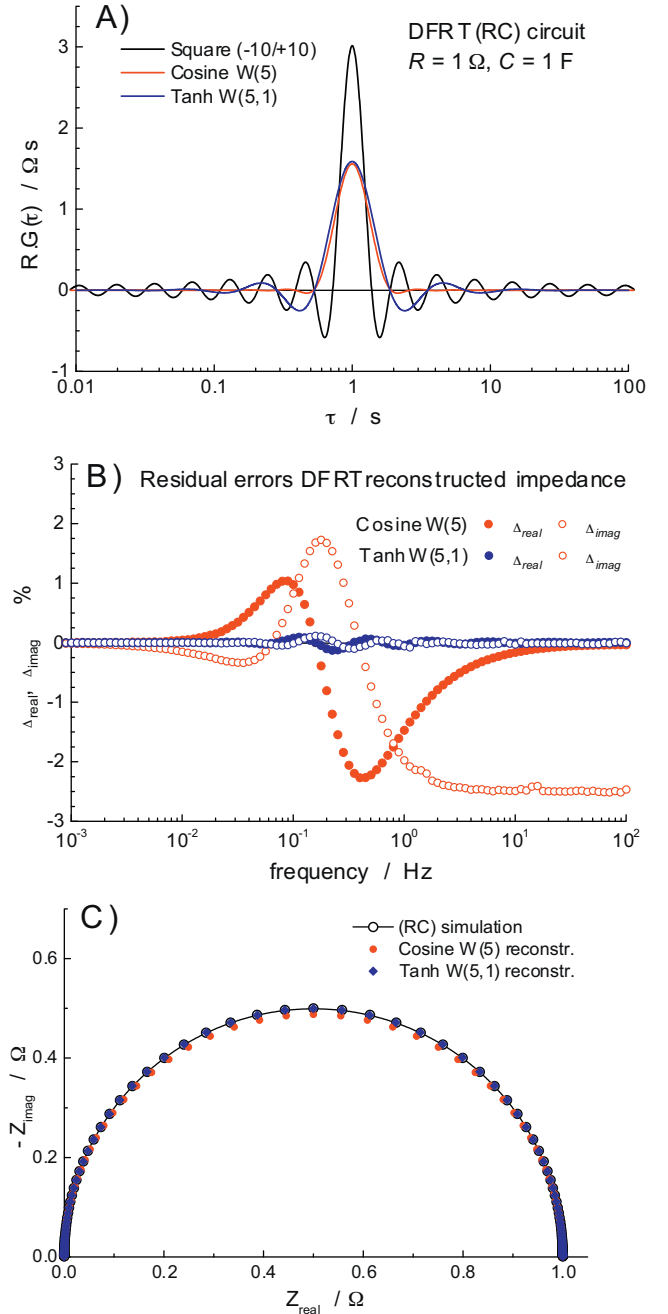$$\approx -Y_0^{-1}\omega^{-n}\sin\frac{n\pi}{2}\Big|_{\omega\to\infty} \tag{13}$$

Fig. 1. *A*) DFRT of a (RC) circuit with a square window ($-10 \le s \le +10$), a Cosine window ($s_{max} = 10$, half height at $s = \pm 5$) and a Tanh window ($\alpha = 5$, $\beta = 1$). *B*) Relative errors for the impedance reconstruction from the DFRT's. *C*) Comparison of the (RC)-simulation with the DFRT reconstructions.
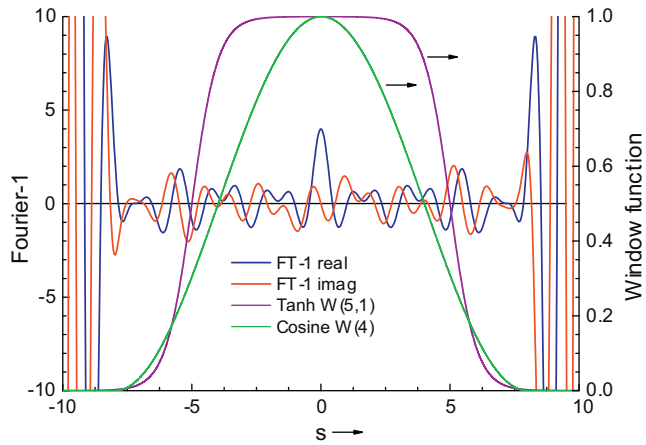
Fig. 2. First Fourier transform of the 3(RQ)-3(RC) model [23]. The Tanh and Cosine windows, used in the inverse transform, are also shown.

and:

$$\omega_{ul}^n = \frac{+\cos\frac{n\pi}{2} + \sqrt{\cos^2\frac{n\pi}{2} + \frac{\Delta_{high}}{1-\Delta_{high}}}}{R \cdot Y_0} \cdot \frac{1-\Delta_{high}}{\Delta_{high}}$$
$$\approx \frac{2\cos\frac{n\pi}{2}}{\Delta_{high}} \cdot highR \cdot Y_0|_{\Delta\to 0} \qquad (14)$$

In this study it was found that a value of $\Delta = 10^{-6}$ was sufficient for proper Fourier transformations and acceptable extrapolation regions. The partial Fourier integral for $-\infty \leq \ln\omega \leq \ln\omega_{ll}$ then becomes:

$$Q_{ll} \int_{-\infty}^{x_{ll}} e^{nx} \cdot e^{-jsx} dx$$
$$= Q_{ll} \cdot e^{nx_{ll}} \left[\frac{n\cos sx_{ll} + s\sin sx_{ll}}{s^2 + n^2} + j\frac{s\cos sx_{ll} - n\sin sx_{ll}}{s^2 + n^2} \right] \qquad (15)$$

with $Q_{ll} = R^2 Y_0 \cdot \sin(n\pi/2)$ and $x_{ll} = \ln\omega_{ll}$. R, Y_0 and n are obtained from the low frequency extension. For the high frequency range,

$\ln\omega_{ul} \leq \ln\omega \leq \infty$ the partial Fourier integral is given by:

$$Q_{ul} \int_{x_{ul}}^{\infty} e^{-nx} \cdot e^{-jsx} dx = Q_{ul} \cdot e^{-nx_{ul}} \left[\frac{n\cos sx_{ul} - s\sin sx_{ul}}{s^2 + n^2} - j\frac{s\cos sx_{ul} + n\sin sx_{ul}}{s^2 + n^2} \right]$$

$$(16)$$

with $Q_{ul} = Y_0^{-1} \cdot \sin(n\pi/2)$ and $x_{ul} = \ln\omega_{ul}$, where R, Y_0 and n now represent the high frequency extension parameters.

2.3. Numerical Fourier transform

The measured data set is extended on both frequency sides, from ω_{ll} to ω_{ul}, using the logarithmic frequency spacing. For this part a numerical Fourier transform is used. The simplest procedure is using the trapezium rule, which basically introduces the same errors as in the FFT. An improvement is a piecewise integration over three consecutive data points using a quadratic function: $y = Ax^2 + Bx + C$ which will follow the contours of the $Z_{im}(\omega)$ more closely. It is easily translated into Fourier segments:

$$\int_{x_i}^{x_{i+2}} (Ax^2 + Bx + C) \cdot e^{-jsx} dx$$
$$= \left[\left(y - \frac{2A}{s^2} \right) \frac{\sin x}{s} + (2Ax + B)\frac{\cos x}{s^2} \right]\Big|_{x_i}^{x_{i+2}}$$
$$- j\left[\left(y - \frac{2A}{s^2} \right) \frac{\cos x}{s} - (2Ax + B)\frac{\sin x}{s^2} \right]\Big|_{x_i}^{x_{i+2}} \qquad (17)$$

with:

$$A = \frac{y_i - y_{i+2}}{x_i - x_{i+2}} - \frac{y_i - y_{i+1}}{x_i - x_{i+1}}] \frac{1}{x_{i+2} - x_{i+1}};$$
$$B = \frac{y_i - y_{i+1}}{x_i - x_{i+1}} - Ax_i - x_{i+1};$$
$$C = Ax_i^2 - Bx_i \qquad (18)$$

Fig. 4. *A*) Relative errors for the reconstructed impedances with the Tanh and Cosine windows. The residual error for the reconstruction with the CNLS-fit and Gauss-approximation is also presented. *B*) Comparison between the simulated data and the two reconstructed impedances.
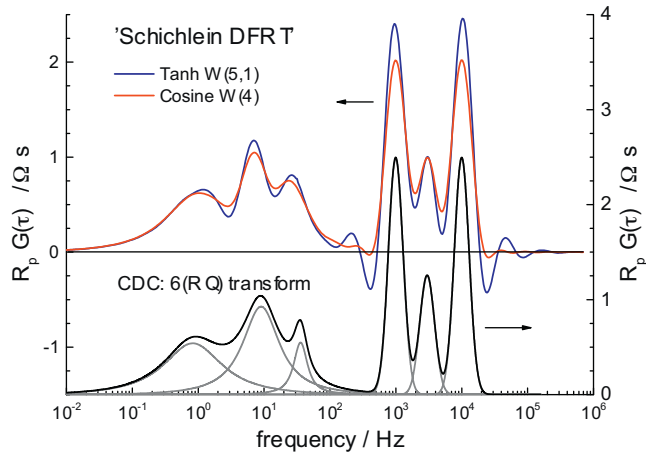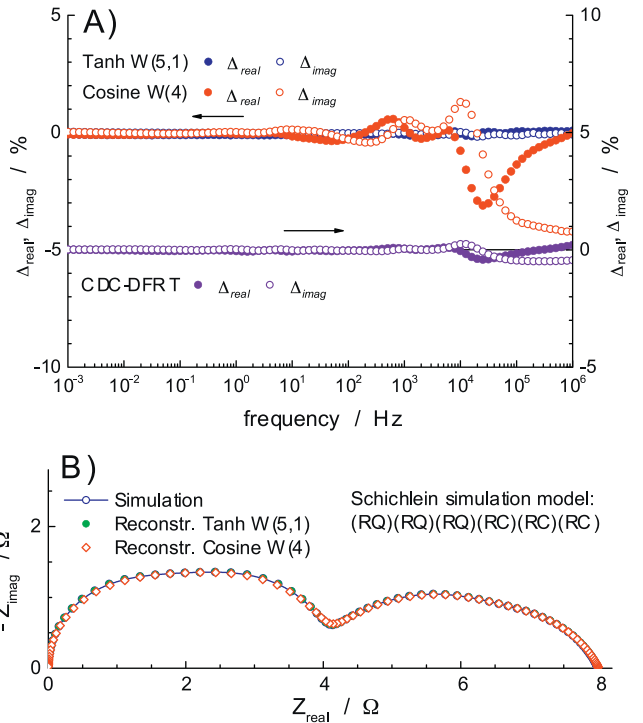

Fig. 3. Upper part: DFRT's obtained from Fig. 2 with both Tanh and Cosine Windows. Lower part: DFRT directly obtained from the 6(RQ) CNLS-fit, where the three δ-functions have been approximated by Gauss-functions. The separate (RQ)-contributions are also presented.
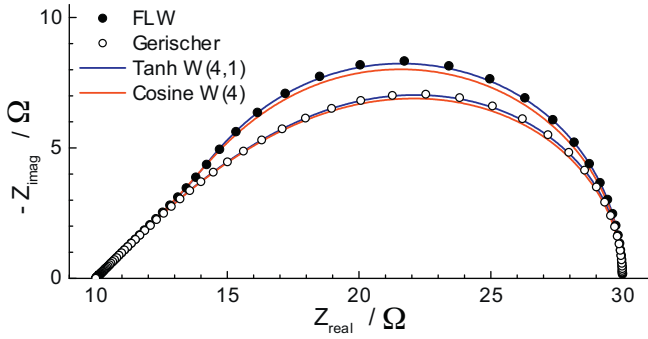
Fig. 5. Impedance representation of the FLW and the Gerischer functions. The reconstructed impedances with both type of windows are also presented.

For $s = 0$ the Fourier transform reduces to:

$$\int_{x_i}^{x_{i+2}} (Ax^2 + Bx + C)dx = \left(\frac{1}{3}Ax^3 + \frac{1}{2}Bx^2 + Cx\right)\Big|_{x_i}^{x_{i+2}} \tag{19}$$

Hence the Fourier transform of $Z_{im}(\omega)$ is divided in three parts: analytically for $-\infty \leq \ln\omega \leq \ln\omega_{ll}$ and $\ln\omega_{ul} \leq \ln(\omega) \leq +\omega$, and numerically between $\ln(\omega_{ll})$ and $\ln(\omega_{ul})$.

2.4. Inverse Fourier transform and DFRT

The Fourier transform of sech(x) is again an analytical function:

$$\int_{-\infty}^{\infty} \text{sech}(x) \cdot e^{-jsx}dx = \frac{\pi}{2}\text{sech}\left(\frac{\pi s}{2}\right) \tag{20}$$

The first Fourier transform, right hand side of Eq. (9) is then simply obtained by division of the numerically obtained $\overline{Z_{im}(\omega)}$, resulting in an optimized $\overline{G(s)}$ function. An inverse Fourier will then produce the DFRT, $R_p \cdot G(\tau)$.

As indicated above, the DFRT of a (RC) circuit results in a δ-function. When the central frequency, ω_0, is made equal to the inverse of the time constant of the (RC) circuit: $\omega_0 = (R \cdot C)^{-1} = \tau_{(RC)}^{-1}$, then the real part of the first Fourier transform, Eq. (6), is a horizontal line at $y = R$, with the imaginary part equal to zero. This results in δ-function for $G(\tau)$. Only the position of τ_0 on the $\ln(\tau)$ axis is accessible, the 'strength', i.e. the surface area, is lost. The actual transformation of Fourier-1 to a DFRT, however, is performed over a limited range of the variable s, in our case:
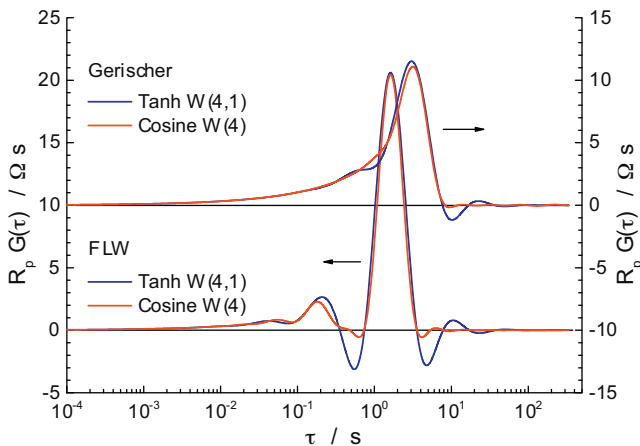
$-10 \leq s \leq 10$. This can be seen as a rectangular window function of the (RC) in the Fourier-1 representation. The second Fourier transform then results in a **sinc**(ln τ) function for $G(\tau)$ which shows disappearing oscillations on both sides of the central peak, see Fig. 1A:

$$R \cdot G(\tau) = \frac{R}{\pi}\frac{\sin(Tln\tau)}{\ln\tau} \tag{21}$$

where $2T$ is the width of the rectangle. Applying a cosine window function (Hann window, [37]), with s_{max} representing the symmetric limits of the window:

$$W(s) = \frac{1}{2}\left(1 + \cos\left(\frac{\pi s}{s_{max}}\right)\right), |s| \leq s_{max}$$
$$W(s) = 0, |s| > s_{max} \tag{22}$$

results in a strong decrease of the oscillations, but also in a factor 2 lower maximum value (Fig. 1A). The shape of this windowed DFRT is given by:

$$R \cdot G(\tau) = \frac{RT}{2\pi}\left\{\frac{\sin(\pi + Tln\tau)}{2(\pi + Tln\tau)} + \frac{\sin(\pi - Tln\tau)}{2(\pi - Tln\tau)} + \frac{\sin(Tln\tau)}{Tln\tau}\right\} \tag{23}$$

and is presented in Fig. 1A as 'Cosine W(5)', i.e. for $s_{max} = 10$.

As generally very strong oscillations are observed at the extremes of the Fourier-1 function, windowing must be applied in order to obtain a useable $G(\tau)$ function. Instead of the Hann windowing function (Eq. 20), a different window function is used in this study which shows a more flat value ($\sim$1) in the central area:

$$\text{Tanh}: W(s) = \frac{(\tanh[\beta(\alpha + s)] + 1)(\tanh[\beta(\alpha - s)] + 1)}{4} \tag{24}$$

α sets the width of the window (at Tanh W(α) = 0.5) and β the steepness of the sides (see Fig. 2 further on). The application to the Fourier-1 of the (RC) transform leads to a DFRT with somewhat more oscillations, but the peak is quite similar to the cosine window as is shown in Fig. 1A. For all three curves in Fig. 1A the area under the $R \cdot G(\tau)$ curve is equal to R. The reconstructions, using Eq. (1), show that the Tanh window introduces a smaller error than the cosine (Hann) window, see the residuals graph in Fig. 1B. Especially the mid-frequency range is affected with the cosine window, as is also visible in the impedance representation in Fig. 1C. From here on the Tanh window function will be abbreviated to Tanh W(α,β), while the cosine or Hann window is presented by Cosine W(T/2), where T/2 is the position of the half height (0.5) with respect to the s-axis (see Fig. 2). The half-height position is

Fig. 6. DFRT's for the FLW (lower part) and Gerischer (upper part) impedances of Fig. 8. The use of both types of window functions is presented.
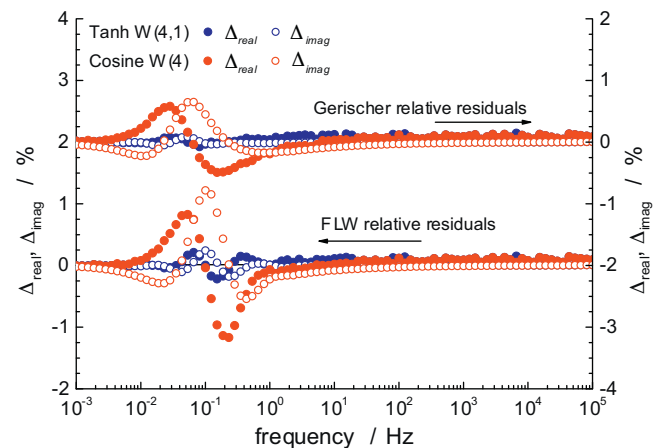

Fig. 7. Relative residuals for the reconstructed impedances for both types of window functions.

Table 1
Parameters for the 6-(RQ) CNLS-fit of the FLW dispersion. $R_\infty = 10\,\Omega$. The fit quality parameter or pseudo $\chi^2 = 9.2 \cdot 10^{-10}$, which signifies a perfect fit. The error estimates are given in percentages. In the last two (RQ) sets the n-power was kept fixed at $n = 1.00$.

Parameter	$(RQ)_1$	$(RQ)_2$	$(RQ)_3$	$(RQ)_4$	$(RQ)_5$	$(RQ)_6$
$R\,[\Omega]$	0.24/82%	0.44/165%	0.61/152%	0.72/60%	1.79/1.8%	16.2/0.01%
$Q\text{-}Y_0\,[S.s^n]$	0.12/53%	0.052/28%	0.052/54%	0.082/50%	0.099/2.3%	0.10/0.02%
$Q\text{-}n\,[-]$	0.497/4%	0.71/20%	0.87/23%	0.98/7%	1.00/fixed	1.00/fixed
$\tau\,[s]$	$8.67 \cdot 10^{-4}$	$4.71 \cdot 10^{-3}$	$1.85 \cdot 10^{-2}$	$5.52 \cdot 10^{-2}$	0.177	1.62

Table 2
Parameters for the 5-(RQ) CNLS-fit of the Gerischer dispersion. $R_\infty = 10\,\Omega$. The fit quality parameter or pseudo $\chi^2 = 3.3 \cdot 10^{-8}$, which signifies a very good fit. The error estimates are given in percentages. In the last two (RQ) sets the n-power was kept fixed at $n = 1.00$.

Parameter	$(RQ)_1$	$(RQ)_2$	$(RQ)_3$	$(RQ)_4$	$(RQ)_5$
$R\,[\Omega]$	1.15/51%	2.07/77%	2.8/47%	4.30/5.5%	9.68/0.86%
$Q\text{-}Y_0\,[S.s^n]$	0.114/25%	0.086/25%	0.14/41%	0.288/7.5%	0.340/1.1%
$Q\text{-}n\,[-]$	0.500/2.5%	0732/12%	0.910/7.8%	1.00/fixed	1.00/fixed
$\tau\,[s]$	0.017	0.094	0.38	1.24	3.3

then equal for both window functions ($\alpha = T/2$). Hence Tanh W(5,1) and Cosine W(5) have the same FWHM (full width = 10 on the s-scale in the Fourier-1).

3. Examples

3.1. Schichlein simulation

Schichlein et al. [23] have demonstrated their transform method with a simulation based on three (RQ)'s and three (RC)'s in series with closely spaced time constants. To test the method presented here this equivalent circuit has been used for the validation test. The impedance spectrum was calculated from 1 mHz to 1 MHz with 10 steps per decade. For the extrapolations, Eqs. (13,14), an (RQ) circuit was fitted to the highest ten frequency points with a pseudo $\chi^2 = 6.7 \cdot 10^{-8}$. For the low frequency extension a R(RQ) circuit was used for the lowest eight frequency sets with a pseudo $\chi^2 = 2.0 \cdot 10^{-11}$. The first Fourier transform and de-convolution was carried out over the range $-10 \le s \le 10$. Both types of window functions were tested, the Tanh window and the cosine window (Hann window, [37]). Fig. 2 shows the results for the Fourier-1, Eq. (9). Both window functions, used in the second transform, are also displayed. Very strong oscillations in both the real and imaginary Fourier transforms are observed at both end

ranges, hence windowing is essential for the reverse Fourier transform.

Fig. 3 shows the conversion to a DFRT for both applied windows. In order to allow comparison with the DFRT presented in [23] a frequency axis has been used. On the right-hand side the three peaks due to the (RC) circuits are found. The window functions have softened the δ-functions to peaks. The Hann window reduces the oscillations that lead to negative contributions. Narrowing the width of the window function decreases these negative contributions, but it also causes the small peak at 3 kHz to disappear. The results compare well with Fig. 4 in the publication by Schichlein et al. [23].

A good test for the quality of the DFRT is performing a reconstruction of the impedance from the DFRT. A relative differences plot shows the compatibility between original data and the DFRT-reconstruct, see the top-part in Fig. 4A. The Tanh-Window function with $\alpha = 5$ and $\beta = 1$, i.e. W(5,1), shows a very good reconstruction, possibly due to allowing some oscillations in the DFRT (Fig. 3, top). The Cosine window, with a somewhat smaller width (Cosine W(4), Fig. 2), clearly leads to moderate deviations at high frequency. One important observation is that setting the window width is not a trivial problem.

This simulated data set has also be analyzed with a CNLS-fit using a series of (RQ)'s. This is not a straightforward analysis, but must be done in a repetitive manner by subsequent partial CNLS-analysis and subtraction (see e.g. [29]). This yielded again a series
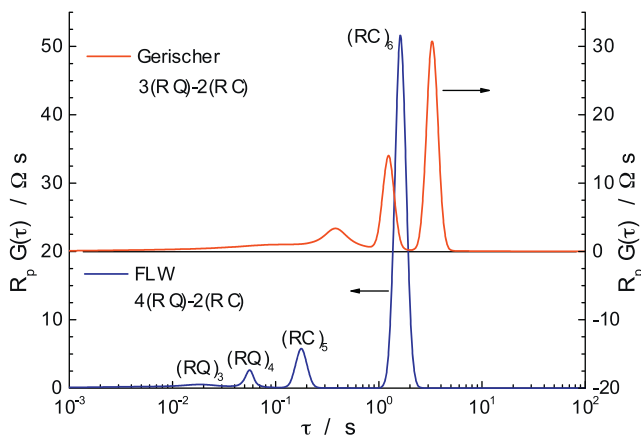
Figure 8. DFRT obtained from a CNLS-fit of a linear combination of (RQ) circuits. The δ-functions were approximated with a Gauss function with W set at 0.15 (see Eq. (6)). For parameter values see Tables 1 and 2.
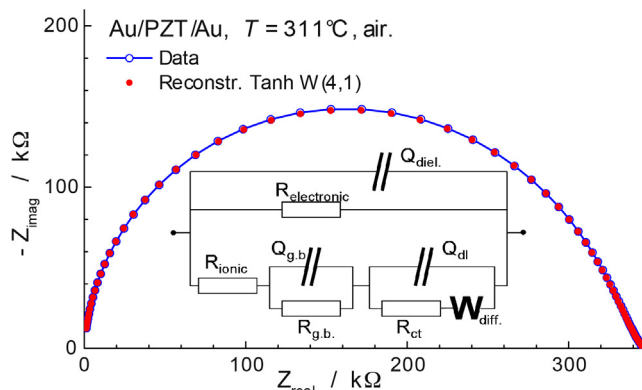
Fig. 9. Impedance of the Au/PZT/Au sample at 311 °C. The inset represents the equivalent circuit used in the CNLS-analysis, see ref. [28]. The reconstruction from the DFRT with a Tanh window is also shown.

Table 3
CNLS-fit results for PZT at 311 °C in air. The KK-test gave $\chi^2_{KK} = 4.6 \cdot 10^{-8}$, indicating very high quality data. The CNLS-analysis resulted in $\chi^2_{CNLS} = 1.1 \cdot 10^{-7}$.

Parameter	value	error
$Q_{diel}, Y_0 [S.s^n]$	$7.46 \cdot 10^{-10}$	0.50%
,, $n [-]$	0.982	0.03%
$R_{electr.} [\Omega]$	$8.65 \cdot 10^4$	0.02%
$R_{ionic} [\Omega]$	$1.21 \cdot 10^5$	2%
$R_{g.b.} [\Omega]$	$4.6 \cdot 10^5$	9%
$Q_{g.b.}, Y_0 [S.s^n]$	$7.6 \cdot 10^{-10}$	5%
,, $n [-]$	0.902	1.40%
$Q_{dl}, Y_0 [S.s^n]$	$4.2 \cdot 10^{-9}$	26%
,, $n [-]$	0.8	5%
$R_{ct} [\Omega]$	$4.4 \cdot 10^6$	30%
$W, Y_0 [S.\sqrt{s}]$	$2.0 \cdot 10^{-8}$	6%

of three (RQ) sets and three (RC)'s. Using the (RQ)-transform formula, together with a Gaussian approximation for the (RC)-contributions, an almost exact DFRT was constructed. A shape factor of $W = 0.15$ was used for the Gauss functions (see Eq. (6). This directly calculated DFRT is also presented in Fig. 3 (lower part). It compares quite well with the Fourier transform DFRT's. Although the Gauss function is an approximation of the δ-function, its influence on the reconstructed impedance is quite small. The reconstructed impedance is very close to the original data set as can been seen in the residuals graph of Fig. 4A (lower part). The deviation in the reconstructed impedance is solely due to the approximation of the δ-functions by (narrow) Gaussians.

3.2. Finite Length Warburg (FLW)

One of the questions is 'is it possible to identify specific transfer functions in the τ-domain?'. The finite length Warburg (FLW, [11]) and the Gerischer impedance [14,16] are quite similar in form, see Fig. 5. At high frequencies a typical Warburg dispersion (i.e. semi-infinite diffusion) is observed for both impedance relations. The low frequency regime shows part of a R(RC) type dispersion. The real differences are in the intermediate frequency ranges. The FLW describes finite length diffusion in a layer with one ideally transferrable boundary for the moving ion (e.g. a corrosion layer). The impedance relation can be given by:

$$Z(\omega)_{FLW} = \frac{Z_0}{\sqrt{j\omega}}\tanh\left(B\sqrt{j\omega}\right) = \frac{Z_0^*}{\sqrt{j\omega\tau}}\tanh\sqrt{j\omega\tau}, \quad (25)$$

with $B = l/\sqrt{D}$, l is the layer thickness and D the chemical diffusion coefficient, $\tau = l^2/D$.

The Gerischer represents semi-infinite diffusion in combination with a side reaction that removes the mobile ion from the diffusion path. As a result it has a finite dc-value, which sets it apart from true semi-infinite length diffusion. The Gerischer can be represented by [14]:

$$Z(\omega)_{Geri.} = \frac{Z_0}{\sqrt{k + j\omega}}, \quad (26)$$

where k is the rate of the side reaction.

Both impedances were simulated between 1 mHz and 100 kHz, with 10 steps per decade. The high-frequency Warburg behavior was identical for both, as was the dc-value for the impedances. The used parameters were: $Z_0 = 10\,\Omega \cdot s^{-1/2}$ for both, $B = 2\,s^{1/2}$ (or $\tau = 4\,s$) and $k = 0.25\,s^{-1}$. A series resistance (electrolyte) of $10\,\Omega$ was added.

Fig. 6 shows the DFRT's obtained with the Fourier transform method described above. There is a marked difference between the DFRT's. The FLW shows a strong peak at $\tau_{max} = 1.6\,s$ with a much smaller peak at about a factor 10 lower τ-value. The Gerischer shows an almost factor two smaller peak at $\tau_{max} = 3.0\,s$, with a more gentile decay for lower τ-values. The Tanh window shows larger negative dips than the Cosine window, but the accuracy for the Tanh window is much better in the reconstruction. This is clearly shown in the relative residuals graph of Fig. 7. The deviations are, however, quite small as can be observed in Fig. 5 where the reconstructions have been added.

A much different picture is obtained with the CNLS-fit approach with a linear set of (RQ) circuits. The FLW could be analyzed with a combination of four (RQ)'s and two (RC)'s with $\chi^2_{CNLS} = 9.2 \cdot 10^{-10}$, which signifies a perfect fit, see Table 1. The Gerischer could be resolved with a combination of three (RQ)'s and two (RC)'s, with $\chi^2_{CNLS} = 3.3 \cdot 10^{-8}$, which is well below the generally observed noise level in experiments, (Table 2). The conversion of these circuits into DFRT's was carried out with the width parameter W for the Gauss functions set at 0.15. The results are presented in Fig. 8. The τ_{max} values for the major peaks coincide well with those of the FT-DFRT, Fig. 6, but the lower τ-part (higher frequency range) deviates significantly from the FT-DFRT. But both methods show a distinct difference between the DFRT's of the FLW and the Gerischer. A first conclusion here is that a DFRT is not necessarily unique, as both the FT-DFRT's and the EqC-constructed DFRT's yield almost the same reconstructed impedances within an acceptable error limit.
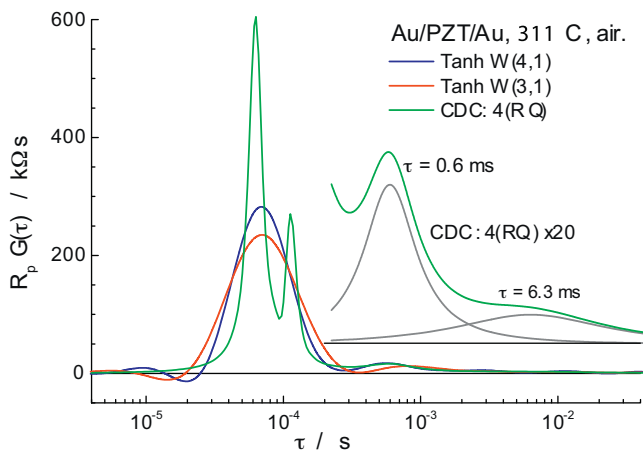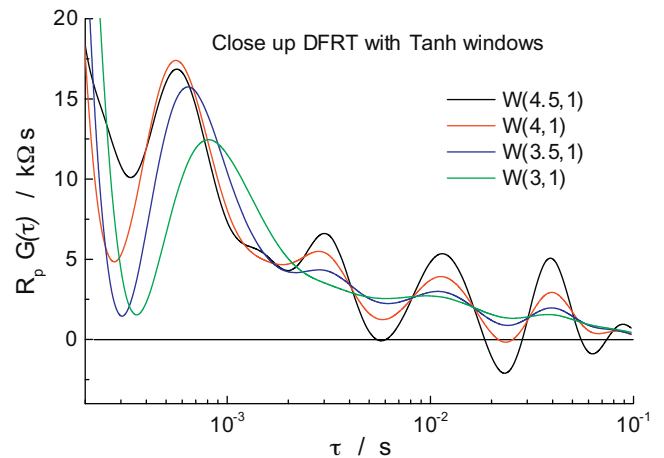

Fig. 10. DFRT for the impedance of Fig. 9 with both a Tanh and a Cosine Window. A DFRT derived from a linear 4-(RQ) fit is also presented.

Fig. 11. Close-up of the DFRT of Fig. 10, showing the oscillations that diminish with decreasing window width.

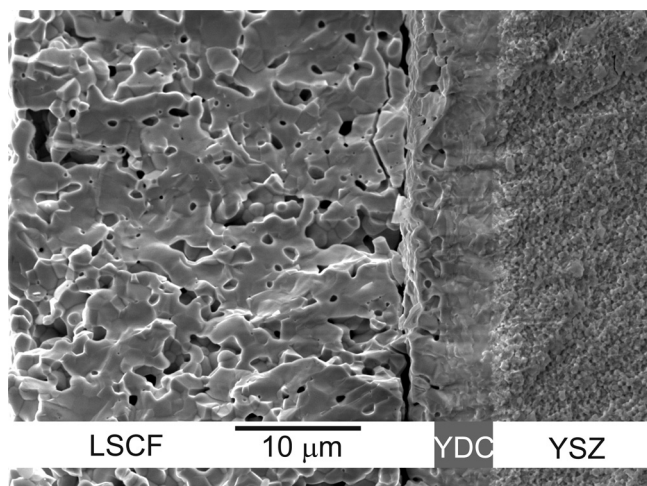**Fig. 12.** Microstructure showing the presence of closed pores for the 'over-sintered' LSCF cathode [30].

Fig. 14. DFRT derived from the impedance of the LSCF cathode of Fig. 13. Results for both window functions are shown, as well as the DFRT derived with the adaptive genetic evolution method (ref. [31,32,38]). The lower part represents the DFRT derived from a linear 5-(RQ) CNLS-fit.

3.3. Finding time constants in the PZT impedance

The EIS study of PZT [28,29] was aimed at determining the mixed conductivity at higher temperatures as function of temperature and oxygen partial pressure. At room temperature the compound is virtually dielectric in nature, starting from about 170 °C, the mixed conductivity becomes measurable. By using ionically blocking gold electrodes, the dc-extrapolation of the low frequency dispersion could be assigned to the electronic conductivity. CNLS-analysis, using a previously described partial-analysis and de-convolution method (see e.g. [6,29]) resulted in a complex equivalent circuit with three parallel conduction path: the electronic, ionic and dielectric rail. This EqC, with eleven independent parameters, is shown in the insert of Fig. 9, the parameter values and error estimates are presented in Table 3. This equivalent circuit could be applied consistently over a wide range of temperatures and pO_2's.

Knowing the number of time constants beforehand would have significantly eased the search for a viable EqC. Hence the question whether the DFRT is capable of indicating the number and positions of relevant time constants. Fig. 9 shows a typical example of the, rather featureless dispersion. The DFRT's, obtained with the Fourier transform method, are presented in Fig. 10 for two different window settings of the Tanh window function. Basically one major peak is shown at $\tau = 6.9 \cdot 10^{-5}$ s, with possibly a minor one at $\tau \sim 0.6 – 0.8$ ms. The DFRT is highly influenced by the window width as is demonstrated in the close-up in Fig. 11. Here a decreasing window width for the Tanh window function shows a dampening of the oscillatory features, but it also shows a shift in the peak position of the minor contribution around $0.6 – 0.8$ ms.

The impedance could also be fitted to a linear series of four (RQ)'s with an excellent $\chi^2_{CNLS} = 9.4 \cdot 10^{-8}$. The resulting DFRT, also shown in Fig. 10, shows two clear peaks at $6.2 \cdot 10^{-5}$ and $1.15 \cdot 10^{-4}$ s and a small contribution at $\tau = 0.6$ ms. There is an even much smaller and broader peak at $\tau = 6.3$ ms. Both small contributions are shown in the insert in Fig. 10, multiplied by a factor 20.

The reconstructed impedance for the Tanh W(4,1) window DFRT matches quite well with the measured data with a $\chi^2_{diff} = 2.7 \cdot 10^{-6}$. With decreasing window width this value increases to $\chi^2_{diff} = 5.2 \cdot 10^{-5}$ for a window setting of Tanh W(3,1). Already a brief conclusion can be made that minor contributions to the DFRT are readily masked by the major peak(s), while these minor contributions can be made visible by a careful
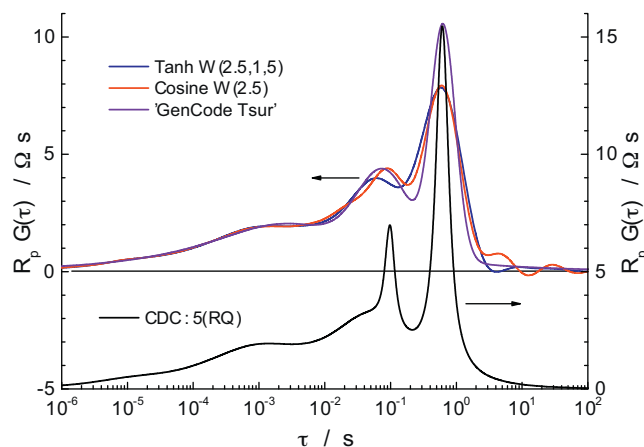
de-convolution process in the frequency domain. The full CNLS-analysis shows still reasonable error estimates for the parameters of these smaller contributions, see Table 3.

3.4. LSCF cathode impedance without simple EqC

Fig. 12 shows the cross section of a $La_{0.6}Sr_{0.4}Co_{0.2}Fe_{0.8}O_{3-\delta}$ (LSCF) cathode sintered at 1300 °C, see Hildenbrand ref. [30]. The sintering temperature of this screen printed cathode is crucial for the performance. At too low temperature (e.g. $T_s = 1100$ °C) the adherence to the electrolyte is too poor, while for $T_s = 1300$ °C the microstructure shows a rather dense layer with a large number of isolated and poorly connected pores. Measurements were performed on a symmetric cell, based on a thin 3 mol% yttria doped tetragonal zirconia electrolyte (TZ3Y) provided on both sides with an yttria doped ceria (YDC) barrier layer.

The impedance, measured at 600 °C in air, is presented in Fig. 13. CNLS-analysis of the impedance did not yield a simple EqC, although the Kramers-Kronig test showed the data to be of high quality with $\chi^2_{KK} = 7.6 \cdot 10^{-8}$ (see also Fig. 15, bottom part). In order to facilitate the low and high frequency extensions of the data (see Section 2.2) the inductance and a small low frequency (RQ) contribution were subtracted from the data file. Including this small contribution would have complicated the low frequency extrapolation. As the interest is in the interpretation of the main dispersion, the subtraction is only a minor modification. This data file was further used in the analysis procedure. Fig. 14 shows the
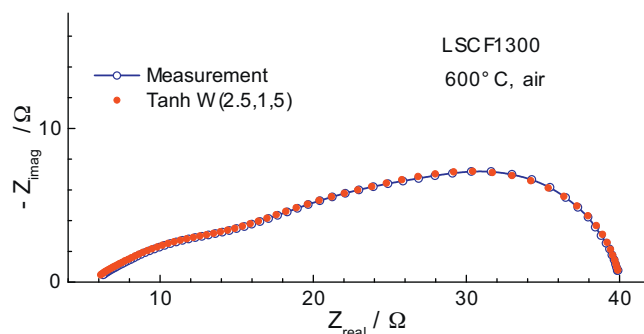

Fig. 13. Measured impedance at 600 °C for the LSCF cathode sintered at 1300 °C. The reconstructed impedance from the DFRT with a Tanh window is also shown.

Table 4

Parameters for the 5-(RQ) CNLS-fit of the LSCF dispersion of Fig. 13. Value for the high frequency cut-off is: $R = 5.80$ (0.14%) [Ω]. The error estimates are presented between parenthesis. The pseudo $\chi^2_{CNLS} = 1.4 \cdot 10^{-7}$, which compares well with the KK-test: $\chi^2_{KK} = 7.6 \cdot 10^{-8}$.

Parameter	$(RQ)_1$	$(RQ)_2$	$(RQ)_3$	$(RQ)_4$	$(RQ)_5$
$R[\Omega]$	1.07/11%	8.80/4.5%	10.7/6.2%	2.42/9.3%	11.3/3.4%
$Q, Y_0 [S \cdot s^n]$	$7.54 \cdot 10^{-4}$/15%	$2.5 \cdot 10^{-3}$/4.0%	0.0131/2.5%	$4.5 \cdot 10^{-2}$/12%	$5.59 \cdot 10^{-2}$/4%
$Q, n[-]$	0.625/3%	0.544/1.7%	0.639/1.7 %	0.950 (fixed)	0.927/0.7%
$\tau_0[s]$	$1.13 \cdot 10^{-5}$	$8.9 \cdot 10^{-4}$	0.046	0.098	0.61

FT- DFRT, using the window function Tanh W(2.5,1.5). For comparison the Cosine W(2.5) DFRT is also shown. These are quite narrow windows, but increasing the size to 3 did result in unwanted oscillations without a clear separation in multiple peaks. Both DFRT's indicate a dominant peak at $\tau = 0.58$ s, a second one at 0.061 s and a very broad distribution around $\tau = 1$ ms. The data set could be analyzed quite well with a linear series of five (RQ) elements with $\chi^2_{CNLS} = 1.4 \cdot 10^{-7}$. Fit parameters are presented in Table 4. The calculated DFRT is shown on the lower part (right hand axis) of Fig. 14. As seen before, direct calculation of the DFRT from this set of (RQ)'s, results in sharper peaks, but the positions coincide almost with the Fourier transform values. The tail for short relaxation times (<10 ms) is almost identical for all DFRT's.

As presented in the introduction, an alternative method is the construction of a DFRT from a 'toolbox of functions' in the τ-domain, by fitting the impedance reconstruction to the measured data. The adaptive genetic evolution analysis, as described by Hershkovitz, Baltianski and Tsur [31,32], is a powerful method to perform both the model search (combination of functions) and the parameter optimization. A thorough analysis by Tsur and Hershkovitz [38] resulted in the combination of two Gauss functions, Eq. (6) and a (RQ) based distribution function, Eq. (5), as best fit with the least number of parameters. The corresponding DFRT, also shown in Fig. 14, shows a somewhat higher main peak, but coincides otherwise quite well with both Fourier transform DFRT's. The parameters for this DFRT are presented in Table 5.

To check the viability of these DFRT's a reconstruction of the impedance was made according to Eq. (1). The reconstruction of the Tanh W(2.5,1.5) DFRT is also shown in Fig. 13. The relative residuals plots are presented in Fig. 15. The bottom graph shows the relative residuals for the Kramers-Kronig test and the CNLS-fit of the five-(RQ) circuit. Here errors are well below 0.2%. The upper part shows the residuals for the three other DFRT's of Fig. 14. Errors are reasonably small, but increase towards the higher frequencies.

The occurrence of a Gaussian distribution can be explained by the electrochemical properties of the pores. Under the ac-perturbation the oxygen activity will also change locally in the electrode. This will cause an exchange between the solid and the gas phase inside the pores, leading to a capacitance:

$$C_{pore} = \left(\frac{4F}{RT}\right)^2 V_{pore} \cdot pO_{2,eq}[F] \qquad (28)$$

Table 5

Parameters resulting from the adaptive genetic evolution method analysis of the LSCF impedance of Fig. 13 (Tsur and Hershkovitz, ref [38]). No error estimates are available.

parameter	Gauss-1	Gauss-2	(RQ)
$R[\Omega]$	9.87	3.24	17.4
W[-]	0.599	1.26	–
$Q, Y_0 [S \cdot s^n]$	––	–	$5.7 \cdot 10^{-3}$
„ n[-]	–	–	0.403
$\tau_0[s]$	0.63	0.0806	$3.16 \cdot 10^{-3}$

with V_{pore} the pore volume and $pO_{2, eq.}$ the equilibrium oxygen partial pressure. It is quite plausible that the pore size distribution shows a Gaussian distribution. Because the number of connected pores is quite small, the bulk diffusion of oxygen becomes one of the important kinetic parameters, which is expressed by the low value of n ($= 0.403$) in the (RQ) component of the overall DFRT from the adaptive genetic evolution analysis.

4. Discussion

The programming of the discussed Fourier transform software has been performed in Borland Delphi (version 7) in double precision. The Fourier-1 array size was 512 data points, evenly spaced from $s = -10$ to $s = +10$. The second transform was done with the same resolution in $\ln(\tau)$. Calculation times were less than a second on a standard PC. A similar Fourier-DFRT procedure could be easily implemented in e.g. Matlab.

An obvious check of the quality of the FT-procedure is that the imaginary part of the second Fourier transform should be zero. For the Tanh window this works very well, generally with $G(\tau)_{im}/G(\tau)_{re} << 10^{-10}$. For the cosine window (Hann window) sometimes considerable deviations were observed (up to a few percent).

4.1. General observations

One of the goals in constructing a DFRT is often to obtain an all-positive distribution function. As has been shown in Section 2.4, for a true capacitive contribution, i.e. a (RC), this is not quite possible, unless a very narrow window function is used. The cosine window significantly attenuates these oscillatory contributions, but as a result the impedance reconstruction shows clear deviations in the residuals graph. The Tanh window function, due to its shape, allows more oscillatory behavior which apparently leads to a more close reconstruction of the impedance (see Figs 1B, 4A and 7).
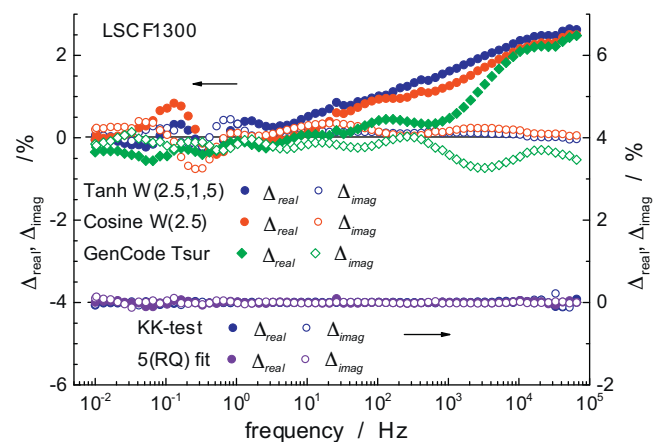

Fig. 15. Error plot for the reconstructed impedances for the LSCF cathode (upper part). The residuals for the original Kramers-Kronig test result and the 5-(RQ) CNLS-fit are shown in the lower part.
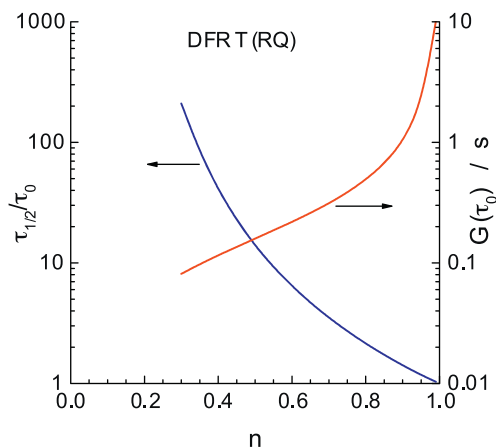
Fig. 16. Relation between the *n*-value of the CPE and the width of the distribution at half maximum, presented as $\tau_{1/2}/\tau_0$. The peak height, as function of *n*, is shown on the right hand axis.

The direct construction of a DFRT from a multi-(RQ) fit shows more pronounced peaks, sometimes even split peaks where the FT-DFRT shows one broad major peak, see Figs 8 and 10. This clearly shows that one cannot consider the FT-DFRT to be unique, as both DFRT's result in an acceptable reconstruction of the impedance. The replacement of the δ-function by a narrow Gauss function has only a small influence on the reconstruction, but the width (*W*-parameter) has a strong influence on the height of the Gauss peak, (comparable to Fig. 16, see below) and hence on the character of the DFRT.

An important point is that small contributions with a relatively wide dispersion (e.g. a Warburg diffusion element or a (RQ) with an *n*-value around 0.5) are not visible in the DFRT, see e.g. Figs 9 and 10. This is easy to understand when one looks at the relation between peak height and the half value width of the DFRT representation in relation with the *n*-value of a (RQ), as presented in Fig. 16. The peak height drops rapidly for a small deviation of *n* from 1. The full width at half height in the ln(τ) graph increases to more than two decades for *n* = 0.5 (diffusion related processes). In general it can be stated that the separation of electrochemical processes in the ln(τ) domain is facilitated by dispersions with comparable strength, i.e. with comparable resistances = area under the $R_p \cdot G(\tau)$ curve, and related *n*-values that are not too small, e.g. in the range 0.7 to 1, see the first example presented in Fig. 3.

4.2. Detection of special dispersion relations

In paragraph 3.2 it was shown that the DFRT's for the FLW and Gerischer showed quite distinct features. It is interesting to see if the Gerischer DFRT is observable in the DFRT's of actual measurements. In a recent report on a La$_2$NiO$_{4+\delta}$ (LNO) cathode a clear Gerischer contribution was found in the CNLS-analysis [39] over all temperatures and pO_2 -values. Fig. 17A shows the impedance of an LNO cathode at 500 °C in air. The two separate contributions, a high frequency R(RQ) circuit and the low frequency Gerischer, are also shown. The chi-squared values for the KK-test and the CNLS-fit were: $\chi^2_{KK} = 5.8 \cdot 10^{-9}$, $\chi^2_{CNLS} = 6.3 \cdot 10^{-9}$. Fig. 17B shows the DFRT for this measurement, obtained with the Fourier-transform method with a Tanh W(4,1) window. For comparison the DFRT for the Gerischer (top of Fig. 6) is also shown. This curve has been shifted on the lnτ axis and normalized to match the peak of the LNO-DFRT. The vertical line in Fig. 17B, noted $\tau_{Geri.}$, presents the position of $(\omega_{max})^{-1}$ in -$Z_{im}(\omega)$ for the Gerischer (with $\omega_{max} = k\sqrt{3}$). The similarity between the two curves is obvious, but the high frequency R(RQ) contribution does

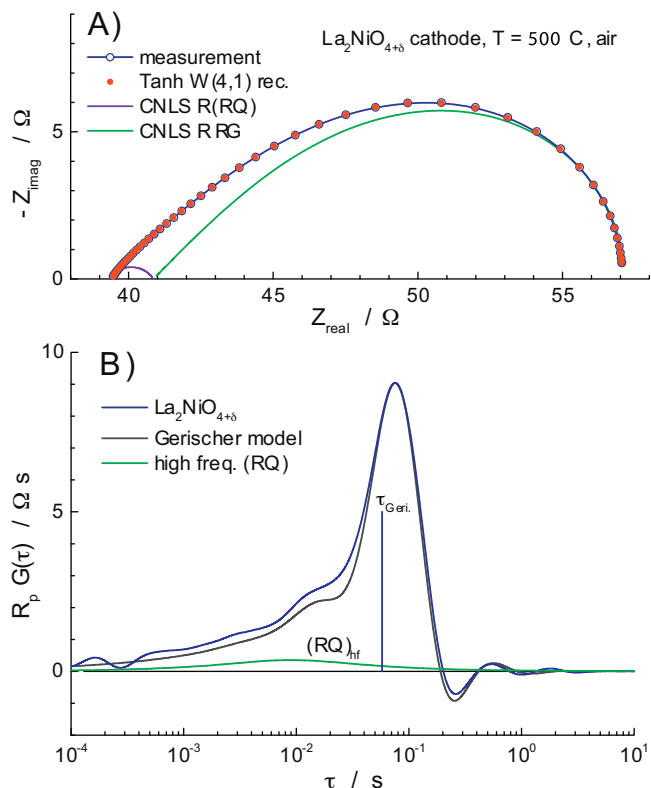**Fig. 17.** A) Impedance of a LNO cathode with a large Gerischer contribution in series with a small high frequency, (RQ)$_{hf}$, contribution. The reconstruction with Tanh W (4,1) is also shown. B) The DFRT for the LNO cathode. For comparison the Gerischer DFRT of Fig. 6 (Tanh Window) is shown. This DFRT is shifted on the lnτ-axis and vertically scaled to match the LNO-DFRT. The separate (RQ)$_{hf}$ function is also shown. The vertical line, τ_{Geri}, denotes the position of $(\omega_{max})^{-1}$ in -$Z_{im}(\omega)$.

not show up. The actual $R \cdot G(\tau)_{(RQ)}$ distribution, calculated with Eq. (5), is also shown in Fig. 17B. It is clear that this contribution in the τ-domain is insignificant, while in the frequency domain (impedance) it has a noticeable contribution to the overall dispersion.

The features of the FLW-DFRT are less pronounced than for the Gerischer-DFRT, see Fig. 6. The side-peaks, that could possibly be characteristic, can easily be masked by other contributions with reasonably small peaks. Here more research is needed to see if the FLW can be directly observed in the DFRT.

4.3. Estimation of time constants and number of parameters.

The first example, the data simulation by Schichlein et al. [23] in Section 3.1, shows clearly all the peak positions of the associated time constants. Even the width of the separate distributions presents an indication of the related *n*-values. But despite the apparent complexity, this example must be considered as a rather ideal situation. As soon as there is quite a difference in magnitude of the separate contributions (especially in the related resistances) the smaller contributions can go unnoticed in the DFRT, see e.g. the examples in Figs 10 and 17. In this case the DFRT does not provide extra information to facilitate the impedance data analysis.

4.4. Alternative methods

The major obstacles with the FT-DFRT method is the necessity for a proper extension at low and high frequencies and the adjustment of the window function which should lead to 'an acceptable' DFRT. For the maximum entropy method and the

Tikhonov regularization the extension is not needed, but setting the smoothing or regularization parameter to an appropriate value is still essential. It would be interesting to compare all these methods for a number of selected problems, but such an undertaking is well beyond the scope of this contribution.

The adaptive genetic evolution method, as derived by Hershkovitz, Baltianski and Tsur [31,32], is an interesting alternative. The DFRT is built up from a selection of distribution functions, e.g. (RQ) representations (Eq. 5), Gaussian or Lorentzian distributions. The reconstruction is then fitted to the original impedance data. This enhances the possibility to arrive at an adequate DFRT without 'smoothing parameters'. But then the necessity evolves to translate these functions into electrochemical or physical processes. Furthermore, in the DFRT a linear contribution of processes is assumed, while in practice often parallel processes are important in the impedance response, see e.g. the example in Section 3.3.

Finally, it is obvious that the FT-DFRT is only suited for systems with a finite dc-resistance. For battery applications or systems with blocking electrodes the dc-limit becomes capacitive. One approach is to model the low frequency part with an appropriate set of transfer functions and subtract the blocking (capacitive) function, which should result in a dc-resistance. This approach has been explored with success by Klotz et al. [40,41]. But in the adaptive genetic evolution procedure the low frequency capacitive dispersion could be modelled in the frequency domain while the main part of the dispersion is resolved in the τ-domain as both come together in the reconstruction of the impedance.

5. Conclusion

From the above presented analysis it is obvious that it is not possible to define the 'true' DFRT for an EIS data set. DFRT's can be useful to compare data sets for a changing extensive parameter (temperature, partial pressure, flow rate, etc.). It is then important to keep the Window-parameter constant (or at least varying in a consistent manner). Similarly, with the adaptive genetic evolution method one needs to use the same set of functions for the complete analysis set as function of the extensive parameters. Furthermore, these functions must have a physical meaning in the impedance or admittance representation.

In retrospect some conclusions seem rather trivial. Nevertheless it is a good thing to follow this investigative path at least once, so that facts can be separated from myth. The DFRT can be a useful instrument in EIS analysis, as has been proven in several publications by the Ivers-Tiffée group [40,41]. DRFT analysis, however, cannot be regarded as a panacea for all problems in EIS-analysis. In fact, often a 'dumb' many-(RQ) based (and hence meaningless) CNLS impedance analysis can be easily transformed to a DFRT in a simple spreadsheet procedure. But its DFRT appearance is often quite different from the one obtained by the Fourier transform method.

The DFRT approach works best for impedances where the various dispersive contributions (sub-circuits) have comparable 'strength' and a not too wide distribution (i.e. an n-value well above 0.5 for a (RQ)-type contribution). The advantage of the DFRT representation is that it clearly shows the major time constants, and to a lesser degree the width of the distribution around these. The bottom line is that much more testing and analysis of the DFRT procedure is needed.

Acknowledgement

References

[1] M. Sluyters-Rehbach, J.H. Sluyters, in: A.J. Bard (Ed.), Electroanalytical Chemistry, vol. 4, Marcel Dekker, New York, 1970, pp. 1–127.

[2] M. Sluyters-Rehbach, J.H. Sluyters, in: E. Yaeger, J.O'M. Bockris, B.E., Conway, S. Sarangapini (Eds.), Comprehensive Treatise of Electrochemistry, vol. 9, Plenum, New York, 1984, p. 177.

[3] J.R. Macdonald, L.D. Potter Jr., A flexible procedure for analyzing impedance spectroscopy results: Description and illustrations, Solid State Ionics 24 (1987) 61–79.

[4] J.R. Macdonald, Impedance spectroscopy: old problems and new developments, Electrochim. Acta 35 (1990) 1483–1492.

[5] B.A. Boukamp, A non-linear least squares fit procedure for analysis of immittance data of electrochemical systems, Solid State Ionics 20 (1986) 31–44.

[6] B.A. Boukamp, A package for impedance/admittance analysis, Solid State Ionics 18-19 (1986) 136–140.

[7] K.E.D. Wapenaar, J. Schoonman, Conductivity enhancement in Ba$_{1-x}$La$_x$F$_{2+x}$ solid electrolytes, Solid State Ionics 5 (1981) 637–640.

[8] J.R. Dygas, G. Fafilek, H. Durakpasa, M.W. Breiter, Automated setup for impedance measurements of electrochemical cells with 2 electrodes, J. Appl. Electrochem. 23 (1993) 553–558.

[9] B.A. Boukamp, Electrochemical Impedance Spectroscopy in Solid State Ionics; Recent Advances, Solid State Ionics 169 (2004) 65–73.

[10] A.D. Franklin, H.J. de Bruin, The Fourier-analysis of impedance spectra for electrode solid electrolytes, Phys.Stat.Sol. -A 75 (1983) 647–656.

[11] D.R. Franceschetti, J.R. Macdonald, R.P. Buck, Interpretation of Finite-Length-Warburg-type impedances in supported and unsupported electrochemical cells with kinetically reversible electrodes, J. Electrochem. Soc. 138 (1991) 1368–1371.

[12] I.D. Raistrick, R.A. Huggins, The transient electrical response of electrochemical systems containing insertion reaction electrodes, Solid State Ionics 7 (1982) 213–218.

[13] A. Honders, G.H.J. Broers, Bounded diffusion in solid solution electrode powder compacts. Part I. The interfacial impedance of a solid solution electrode (M$_x$SSE) in contact with a m$^+$-ion conducting electrolyte, Solid State Ionics 15 (1985) 173–183.

[14] B.A. Boukamp, H.J. Bouwmeester, Interpretation of the Gerischer impedance in solid state ionics, Solid State Ionics 157 (2003) 29–33.

[15] B.A. Boukamp, M. Verbraeken, D.H.A. Blank, P. Holtappels, SOFC-anodes, proof for a finite-length type Gerischer impedance? Solid State Ionics 177 (2006) 2539–2541.

[16] Y. Lu, C. Kreller, S.B. Adler, Measurement and modeling of the impedance characteristics of porous La$_{1-x}$S$_r$xCoO$_{3-\delta}$ electrodes, J. Electrochem. Soc. 156 (2009) B513–B525.

[17] P.H. Bottelberghs, H.H.J. Broers, Interfacial impedance behaviour of polished and paint platinum electrodes at Na$_2$WO$_4$-Na$_2$MoO$_4$ solid electrolytes, J. Electroanal. Chem. 67 (1976) 155–167.

[18] S. Havriliak, S. Negami, A complex plane representation of dielectric and mechanical relaxation processes in some polymers, Polymer 8 (1967) 161–210.

[19] E. Barsoukov and J. R. Macdonald, editors, Impedance Spectroscopy: Theory, Experiment, and Applications, 2nd Edition, John Wiley & Sons, Hoboken, NJ, 2005.

[20] M.E. Orazem, B. Tribollet, Electrochemical Impedance Spectroscopy, John Wiley Sons, Hoboken, 2008.

[21] V.F. Lvovich, Impedance Spectroscopy. Applications to Electrochemical and Dielectric Phenomena, John Wiley & Sons, 2012.

[22] A. Lasia, Electrochemical Impedance Spectroscopy and its Applications, Springer New York/Heidelberg, 2014.

[23] H. Schichlein, A.C. Müller, M. Voigts, A. Krügel, E. Ivers-Tiffée, Deconvolution of electrochemical impedance spectra for the identification of electrode reaction mechanisms in solid oxide fuel cells, J. Appl. Electrochem. 32 (2002) 875–882.

[24] T. Hörlin, Maximum entropy in impedance spectroscopy of non-inductive systems, Solid State Ionics 67 (1993) 85–96.

[25] T. Hörlin, Deconvolution and maximum entropy in impedance spectroscopy of noninductive systems, Solid State Ionics 107 (1998) 241–253.

[26] J. Macutkevic, J. Banys, A. Matulis, Determination of the distribution of the relaxation times from dielectric spectra, Nonlinear Anal. Model. Control 9 (2004) 75–88.

[27] M. Saccoccio, T.H. Wan, C. Chen, F. Ciucci, Optimal Regularization in Distribution of RelaxationTimes applied to Electrochemical Impedance Spectroscopy: Ridge and Lasso Regression Methods–A Theoretical and Experimental Study, Electrochimica Acta 147 (2014) 470–482.

[28] B.A. Boukamp, M.T.N. Pham, D.H.A. Blank, H.J.M. Bouwmeester, Ionic and electronic conductivity in lead-zirconate-titanate (PZT), Solid State Ionics 170 (2004) 239–254.

[29] B.A. Boukamp, D.H.A. Blank, 'High precision' impedance spectroscopy: a strategy demonstrated on PZT, IEEE-TUFFC 58 (2011) 2521–2530.

[30] N. Hildenbrand, Improving the electrolyte-cathode assembly for mt-SOFC, Thesis, University of Twente, the Netherlands (2011), ISBN: 978–94-91211–57-7.

[31] S. Hershkovitz, S. Baltianski, Y. Tsur, Harnessing evolutionary programming for impedance spectroscopy analysis: A case study of mixed ionic-electronic conductors, Solid State Ionics 188 (2011) 104–109.

[32] S. Hershkovitz, S. Baltianski, Y. Tsur, Electrochemical impedance analysis of SOFC cathode reaction using evolutionary programming, Fuel Cells 12 (2012) 77–85.

[33] B.A. Boukamp, A linear Kronig-Kramers transform test for immittance data validation, J. Electrochem. Soc. 142 (1995) 1885–1894.

[34] K.S. Cole, R.H. Cole, Dispersion and absorption in dielectrics - I Alternating current characteristics, J. Chem. Phys. 9 (1941) 341–352.

[35] F. Dion, A. Lasia, The use of regularization methods in the deconvolution of underlying distributions in electrochemical processes, J. ElectroAnal. Chem. 475 (1999) 28–37.

[36] B.A. Boukamp, Practical application of Kramers-Kronig transforms on impedance measurements in solid state electrochemistry, Solid State Ionics 62 (1993) 131–141.

[37] S.D. Stearns, Digital signal analysis, Hayden Book Company, New Jersey, 1975, pp. p93.

[38] Y. Tsur and S. Hershkovitz, private report,(2010).

[39] N. Hildenbrand, P. Nammensma, D.H.A. Blank, H.J.M. Bouwmeester, B.A. Boukamp, Influence of configuration and microstructure on performance of $La_2NiO_{4+\delta}$ IT-SOFC cathodes, J. Power Sources 238 (2013) 442–453.

[40] D. Klotz, Characterization and modelling of electrochemical energy conversion systems by impedance techniques, Thesis, Karlsruh Institute for Technology (2012), ISBN 978–3-86644–903-9.

[41] D. Klotz, J.P. Schmidt, A. Kromp, A. Weber, E. Ivers-Tiffée, The distribution of relaxation times as beneficial tool for equivalent circuit modeling of fuel cells and batteries, ECS Transactions 41 (2012) 25–33.